

Enhanced Optical ^{13}C Hyperpolarization in Diamond Treated by High-Temperature Rapid Thermal Annealing

Max Gierth, Valentin Krespach, Alexander I. Shames, Priyanka Raghavan, Emanuel Druga, Nicholas Nunn, Marco Torelli, Ruhee Nirodi, Susan Le, Richard Zhao, Alessandra Aguilar, Xudong Lv, Mengze Shen, Carlos A. Meriles, Jeffrey A. Reimer, Alexander Zaitsev, Alexander Pines, Olga Shenderova, and Ashok Ajoy*

Methods of optical dynamic nuclear polarization open the door to the replenishable hyperpolarization of nuclear spins, boosting their nuclear magnetic resonance/imaging signatures by orders of magnitude. Nanodiamond powder rich in negatively charged nitrogen vacancy defect centers has recently emerged as one such promising platform, wherein ^{13}C nuclei can be hyperpolarized through the optically pumped defects completely at room temperature. Given the compelling possibility of relaying this ^{13}C polarization to nuclei in external liquids, there is an urgent need for the engineered production of highly “hyperpolarizable” diamond particles. Here, a systematic study of various material dimensions affecting optical ^{13}C hyperpolarization in diamond particles is reported on. It is discovered surprisingly that diamond annealing at elevated temperatures $\sim 1720^\circ\text{C}$ has remarkable effects on the hyperpolarization levels enhancing them by above an order of magnitude over materials annealed through conventional means. It is demonstrated these gains arise from a simultaneous improvement in NV^- electron relaxation/coherence times, as well as the reduction of paramagnetic content, and an increase in ^{13}C relaxation lifetimes. This work suggests methods for the guided materials production of fluorescent, ^{13}C hyperpolarized, nanodiamonds and pathways for their use as multimodal (optical and magnetic resonance) imaging and hyperpolarization agents.

1. Introduction

The development of quantum sensors over the past decade has heralded new opportunities for harnessing the power of quantum technologies in the real world. This includes, for instance, the ultrasensitive probing of magnetic^[1] and electric fields,^[2] as well as temperature^[3,4] and inertial rotations.^[5,6] The workhorse platform of this class has been the negatively charged nitrogen-vacancy NV^- defect center in diamond, driven by the exquisite room-temperature coherence time of its electronic spin, along with the dual ability to spin polarize and interrogate it through optical means.^[7]

Particulate forms of NV-center endowed diamond “quantum materials” portend additional applications that stem from their inherently high surface area and targeting ability through surface functionalization.^[8,9] Nanodiamond (ND) particles, for instance, can be served as deployable and “in cell” quantum sensors.^[4,10–12] An exciting emerging application involves harnessing

M. Gierth, V. Krespach, P. Raghavan, E. Druga, R. Nirodi, S. Le, R. Zhao, A. Aguilar, X. Lv, M. Shen, Prof. A. Pines, Prof. A. Ajoy
Department of Chemistry
University of California
Berkeley, CA 94720, USA
E-mail: ashokaj@berkeley.edu


Dr. A. I. Shames
Department of Physics
Ben-Gurion University of the Negev
Be'er-Sheva 8410501, Israel
N. Nunn, Dr. M. Torelli, Dr. O. Shenderova
Adamas Nanotechnologies, Inc.
8100 Brownleigh Dr, Suite 120, Raleigh, NC 27617, USA

Prof. A. Zaitsev
College of Staten Island
CUNY
2800 Victory Blvd., Staten Island, NY 10312, USA

Prof. A. Zaitsev
Gemological Institute of America
50 W 47th, New York, NY 10036, USA

Prof. C. A. Meriles
Department of Physics and CUNY-Graduate Center
CUNY-City College of New York
New York, NY 10031, USA

Prof. J. A. Reimer
Department of Chemical and Biomolecular Engineering, and
Materials Science Division, Lawrence Berkeley National Laboratory
University of California
Berkeley, CA 94720, USA

 The ORCID identification number(s) for the author(s) of this article can be found under <https://doi.org/10.1002/qute.2020000050>

DOI: 10.1002/qute.2020000050

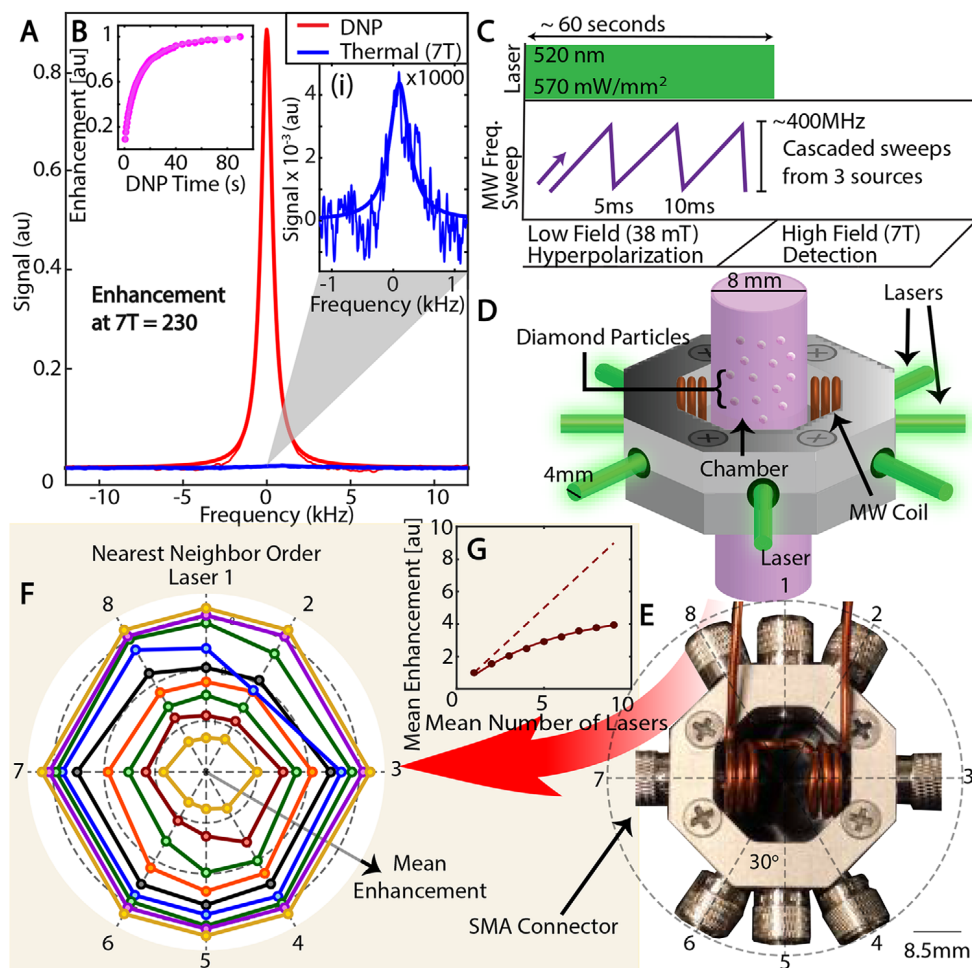


Figure 1. Room temperature optical hyperpolarization. A) Typical ^{13}C hyperpolarization, shown here for HTA optimized $18\ \mu\text{m}$ diamond particles. Red (blue) line shows the DNP (7 T thermal signal, zoomed in inset (i)), a signal enhancement here $\varepsilon = 230$ with respect to 7 T. B) Polarization buildup curve, showing DNP saturation in ≈ 60 s. C) Schematic of DNP protocol involving optical pumping at low magnetic fields (≈ 38 mT) under simultaneous chirped MW irradiation. ^{13}C NMR is subsequently detected at 7 T. D, E) Hyperpolarization setup. Laser excitation is via multimode 1 mm core optical fibers (≈ 800 mW) arranged in an octagon, with an additional collimated laser applied from the bottom. Beam diameters are ≈ 4 mm at point of contact with the diamond particle sample, which is carried in a test tube and under water. F) Hyperpolarization homogeneity in a 20 mg sample upon application of nearest-neighbor (NN) combinations of excitation lasers arranged on the octagonal ring. Polar plot (r, θ) axes refer to enhancement $C_{k, \dots, k+N}$ and excitation angle of the k th laser, respectively. Approximately circular buildup indicates spatially homogeneous polarization in the sample (lines). Slight deviations from circularity arise due to experimental imperfections (MW inhomogeneity). G) DNP scaling with number of lasers (C_N), considering application of an increasing order of NN laser combinations. Sublinear growth indicates uniform polarization that is not laser power limited.

lattice ^{13}C nuclear spins in these diamond particles as an auxiliary resource. Particularly attractive is the hyperpolarization of these ^{13}C nuclei via the optically pumped NV centers, placing them in athermal spin configurations that have greatly enhanced nuclear magnetic resonance (NMR) signatures.^[13] The ^{13}C NMR signal can often be enhanced by several orders of magnitude, in a manner completely independent of particle orientation, with the hyperpolarization being carried out at room temperature and with relatively benign resources. Indeed, such optical methods for dynamic nuclear polarization (DNP)^[14,15] present several advantages over conventional methods involving cryogenic temperatures and large magnetic fields,^[16] since the hyperpolarization can be generated replenishably and under ambient conditions and with modest resources (low optical and microwave

powers).^[17,18] As a representative example, **Figure 1A** demonstrates small $18\ \mu\text{m}$ microparticles having large nuclear polarization levels $\approx 0.28\%$ in just under a minute of optical pumping. This corresponds to a gain of ≈ 230 over their Boltzmann polarization at high field (7 T) (4×10^5 over the polarization at a polarizing field of 38 mT), and to a million-fold time acceleration of imaging these particles in MR imaging.^[19] Several compelling applications open as a result. The optical pumping leads to an associated, simultaneous, bright fluorescence from the NV^- centers that is non-blinking and non-bleaching. Harnessing the dual-mode bright nature of these particles in both the optical as well as MR domains opens new avenues for them to serve as imaging agents in disease diagnostics and monitoring.^[19,20] Moreover, nanodiamond particles

inherently possess large surface areas ($\approx 57 \text{ m}^2 \text{ g}^{-1}$ for 100 nm particles^[21]), and along with the long lifetimes of the ^{13}C spins, allow hyperpolarized surface ^{13}C nuclei to serve as spin polarization relay channels to external nuclear spins. One could envision, for instance, a liquid coating on the particles being spin-polarized via the surface nuclei through Overhauser contact.^[22]

While the gains in hyperpolarization can be impressive, experience indicates that material factors play a key role in ultimately setting the obtained ^{13}C polarization levels. This comes as no surprise; indeed, there has been tremendous progress in the last decade in fabricating diamond particles that are materials-optimized for fluorescence brightness.^[23–25] This includes diamond growth, e-irradiation, and annealing conditions, that have enabled diamond particles to become some of the brightest and most photostable targetable fluorescent agents available.^[26] However, analogous optimization of material conditions for optical hyperpolarization is several-fold more challenging. Apriori, it is uncertain if conditions that produce optically brightest particles (typically few ppm of NV^- center concentration and annealing at 850°C) are also those that make them maximally NMR bright. A rich confluence of factors dictate at once the buildup of ^{13}C hyperpolarization, and optimized materials are contingent on having high initial polarization and long coherence times on the NV^- electron (source), along with a long lifetime on the ^{13}C nuclei (target). These, in turn, are strongly determined by interactions with paramagnetic impurities and lattice distortions. No doubt, these factors are quite different from conditions for radical-induced hyperpolarization at cryogenic conditions.^[27]

In this paper, we unravel the various material dimensions that govern optical ^{13}C hyperpolarization in diamond particles. We accomplish this through combined electron paramagnetic resonance (EPR) and NMR relaxometry studies, along with probes of hyperpolarization buildup and decay behavior for over 30 samples, produced with controllably engineered electron irradiation and annealing conditions. We focus on high-pressure high-temperature (HPHT) diamond particles,^[28] given their relative ease of production at scale. To distill effects from each material dimension separately, we consider particles fabricated from identical starting parent materials. While confirming the critical effect of the lattice quality to ultimate ^{13}C hyperpolarization levels, we discover a surprising new effect upon sample high-temperature annealing (HTA) for 15 min at $\approx 1720^\circ\text{C}$, which enables a large boost in the hyperpolarization levels, in some cases by over an order of magnitude compared to conventional diamond fabrication. Our data reveals the intriguing origins of these gains, including the crucial role played by paramagnetic impurities in bounding both the electronic as well as the nuclear lifetimes.

2. High Mass ^{13}C Hyperpolarization

We consider type Ib HPHT particle samples (Hyperion) with identical ≈ 100 ppm nitrogen content and compare their relative performance for room temperature DNP at $B_{\text{pol}} \approx 38$ mT, close to the optimal field for hyperpolarization (see Methods in Supporting Information). The particles (all at natural abundance ^{13}C) are illuminated with 520 nm laser light to initialize the NV^- electrons to the $m_s = 0$ state, and subjected to chirped microwave (MW) irradiation over the NV^- EPR spectrum to

transfer polarization to the ^{13}C lattice (see Figure 1).^[17,29] Note that, in this paper, we will refer to the NV center as being in its negatively charged state, and ignore effects of charge dynamics. Figure 1B shows typical hyperpolarization buildup curve, saturating in ≈ 90 s of optical pumping. Polarization transfer under the MW sweeps (Figure 1C) proceeds through a sequence of rotating frame Landau–Zener transitions^[30] to relatively weakly coupled ^{13}C nuclei, and subsequent spin-diffusion serves to homogenize the polarization in the bulk lattice. Interactions of the ^{13}C nuclei with other lattice spins, especially paramagnetic impurities, contribute to the leakage of polarization to unmeasurable degrees of freedom that effectively manifests as T_1 relaxation, bounding the overall polarization level.

Experimentally, the hyperpolarized ^{13}C NMR signals are measured at high field (7 T), accomplished by rapidly shuttling the sample prior to measurement. Benchmarking the hyperpolarization level of each sample against its counterpart 7 T Boltzmann value is unwieldy and time-consuming, since a typical thermal measurement takes over 30 h for discernible SNR, limited by low sample filling factor ($\lesssim 10^{-2}$) in detection. Instead here, we adopt an alternate strategy. For a fair comparison, we mass normalize the hyperpolarization signals from the various samples and benchmark each sample against the unit mass thermal NMR signal at 7 T. We report these DNP enhancement factors, henceforth labeled ϵ , which correspond to absolute polarization levels $\approx 0.1\epsilon\%$.

Technically, to ensure the entire mass (5–30 mg) of the diamond particles (occupying $\lesssim 18 \text{ mm}^3$ volume immersed in water) is polarized uniformly, we employ a laser illumination geometry that serves to penetrate all particle facets and ensure homogenous powder polarization in spite of scattering and penetration losses. This is accomplished by using eight 800 mW fiber-coupled lasers arranged along an octagonal ring, along with another collimated laser that excites the sample from the bottom, approximating a hemispherical excitation pattern (see Figure 1D,E). The optical excitation ($\approx 570 \text{ mW mm}^{-2}$) is minimally obstructed by the MW coil, which is a split-solenoid of 9 mm diameter (see Figure 1E), and with an exceedingly low MW power density ($\approx 2.5 \text{ mW mm}^{-3}$). To quantify the effectiveness of this excitation geometry, consider that, for instance, C_{k_1, k_2} refers to the obtained DNP enhancement employing laser numbered k_1 and k_2 on the octagonal ring together. We now consider (Figure 1F) the DNP signal under nearest-neighbor (NN) combinations of the laser beams, $C_k, C_{k,k+1}, \dots, C_{k, \dots, k+N}$, where $k \in [1, 8]$ is the laser number on the ring (see Figure 1E), and N refers to the NN order. The inner yellow line in Figure 1F, for instance, refers to $N = 1$ (single lasers), the red line to $N = 2$ (NN pairs), and the green points to $N = 3$ (NN triples). DNP levels here are shown in a polar plot, where the radius indicates the obtained signals, and the angular coordinate represents laser k above. The approximately circular ring-like patterns in Figure 1F demonstrates the spatially homogeneous buildup of polarization in the powder samples. The slight deviations from circularity can be ascribed to MW inhomogeneity due to the MW coil being off-center with respect to the lasers. Figure 1G finally illustrates the mean signal obtained for each NN laser order, $\langle C_N \rangle = \langle C_{k, \dots, k+N} \rangle = \frac{1}{8} \sum_j C_{k_j, \dots, k_j+N}$; the sublinear scaling in Figure 1G demonstrates that the DNP in the ≈ 20 mg mass is not laser-limited. In the Supporting

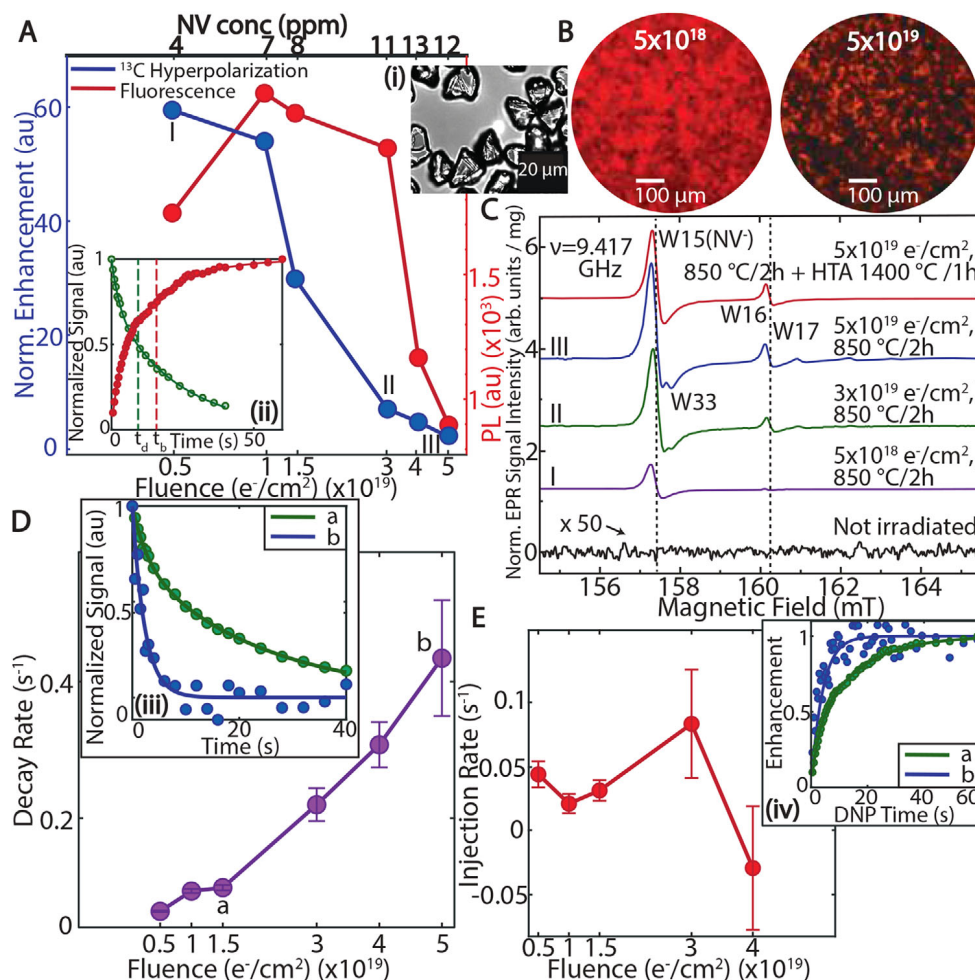


Figure 2. DNP scaling with electron irradiation dose. A) Mass normalized hyperpolarization enhancements for 18 μm particles at ≈ 38 mT (blue line) showing steep decrease at high irradiation fluences. Corresponding NV^- concentrations are denoted on upper axis (bold). Red line shows optical fluorescence and displays a similar trend. Inset (i): particle micrograph showing particle size $18 \mu\text{m} \pm 3 \mu\text{m}$. Inset (ii): representative polarization buildup (red) and decay (green) curves. Buildup t_b and decay t_d times are denoted by respective $1/e$ intercepts. B) Fluorescence micrographs of representative samples marked in (A) demonstrating differences in optical brightness. C) X-band EPR spectra. Growth of NV^- center (W15) peaks at larger electron fluences is associated with an increase in additional triplet paramagnetic defects (here triplet centers W33, W16-17) (see also Figure 3). D) Polarization decay rates for the samples considered in (A). Inset (iii): representative polarization decay curves for low and high electron dose samples. E) Polarization injection rate extracted from the buildup curves. Deleterious effects on both the polarization injection and decay rates at high electron fluences lead to reduced hyperpolarization efficiency. Inset (iv): polarization buildup curves for representative samples in (D).

Information, we also study the correlation between pairs of lasers situated on the octagonal ring, measuring $\langle C_{k,k+n} \rangle = \frac{1}{8} \sum_j C_{k_j,k_{j+n}} / (C_{k_j} + C_{k_{j+n}})$, the mean value of the DNP enhancement on applying two lasers separated by n simultaneously, and normalized by the effect of them both applied separately. We find that (see Supporting Information), to a good approximation, the different lasers contribute to hyperpolarization in different parts of the sample volume, and the near hemispherical excitation leads to uniform polarization buildup.

3. Effects of Increasing Electron Fluence

First, considering the effects of particle size by studying particles obtained through milling identical starting materials, we find a decrease in hyperpolarization levels at small particle sizes,

100 nm particles performing worse by about an order of magnitude compared to 18 μm particles (see Supporting Information). However, since this is strongly conditioned on the harder to control material degradation due to milling, we will consider a more systematic study elsewhere. Instead, for clarity, we focus here almost completely on diamond particles that are identically milled to a uniform size $18 \pm 3 \mu\text{m}$, all starting from the same parent material. We consider in Figure 2 samples prepared under varying fluences of electron irradiation and standard annealing conditions (850°C for 2 h), both of which can be precisely controlled. Naively, the increasing fluence results in an increasing NV^- center concentration that should seed a greater polarization in the ^{13}C lattice. Practically, however, this is associated with concomitant lattice damage, as well as an increased paramagnetic defect concentration, resulting in a decrease in ^{13}C T_1 times, and manifests as an inherent tradeoff in the hyperpolarization levels with

fluence. This is evident in the experiments in Figure 2A where we observe a DNP optimum at $\approx 5 \times 10^{18} \text{ e cm}^{-2}$, which we estimate from EPR data to correspond to an NV^- concentration of $\approx 4 \text{ ppm}$ (upper axis). Furthermore, the DNP enhancements correlate with the optical brightness of the particles (red line in Figure 2A), which also decreases at higher fluences, here due to the generation of paramagnetic optical traps. Figure 2B, for instance, shows representative micrographs taken under a 617 nm long-pass filter highlighting the relative particle brightness.

Continuous wave X-band (9.4 GHz) EPR measurements (at room temperature) highlight underlying lattice conditions responsible (Figure 2C). We calibrate g -factors and densities N_s of paramagnetic $S = 1/2$ species against a reference sample of purified detonation nanodiamond (ND) powder with $g = 2.0028(2)$ and $N_s = 6.3 \times 10^{19} \text{ spins g}^{-1}$.^[31] Spectra recorded in the half-field ($g = 4$) region allow reliable quantification of NV^- (W15) triplet centers, tracking EPR lines originating from forbidden ($\Delta m_s = 2$) transitions between triplet state Zeeman levels. Figure 2C illustrates that increasing electron fluence leads to the growth of $g = 4.274(5)$ NV^- center signals; and while at low fluences ($5 \times 10^{18} \text{ e cm}^{-2}$), the NVs dominate the spectrum, higher fluences are associated with the appearance and strengthening of additional signals, here attributable to W16–W18 and W33 triplet defect centers. We emphasize that for clarity, the spectra in Figure 2C focus on the spectral region close to the NV^- peaks, and do not show the primary lattice paramagnetic defects which also change in concentration (see Figure 4C and Supporting Information).

The presence of paramagnetic spins bottlenecks hyperpolarization buildup in the high e-fluence samples. Indeed, the saturation hyperpolarization values reflect a dynamic equilibrium between NV^- -induced polarization injection into the lattice ^{13}C nuclei, and its inherent decay due to nuclear T_1 processes. If β_i and β_d denote the (assumed monoexponential) polarization injection and decay rates, respectively, the buildup curve (Figure 2A(ii)) has the functional form, $\epsilon(t) = \frac{\beta_i}{\beta_i + \beta_d} [1 - e^{-(\beta_i + \beta_d)t}]$. Hence for each sample, measurement of the polarization buildup and decay curves allows an independent estimation of injection and decay rates. Both parameters provide valuable insight into the material conditions that affect hyperpolarization levels; if for instance β_d is large, polarization saturates at a low value in spite of high NV^- concentrations. The buildup and decay curves are, however, in general, weakly bi-exponential (see Figure 2A) on account of disparate behavior between directly NV^- -coupled ^{13}C and weaker bulk nuclei. We can nonetheless, to a good approximation, quantify the buildup and decay rate constants (and error bars) through the inverse $(1 - 1/e)$ and $1/e$ intercepts of the fitted lines, respectively, depicted as t_b , t_d in Figure 2A. This provides a faithful reflection of the underlying injection rates, although carrying larger error in the limit of $T_1 \rightarrow 0$.

The extracted ^{13}C relaxation rates grow steeply for the high e-fluence samples (Figure 2D), and as the representative decay curves from low and high fluence samples in Figure 2D(iii) indicate, the differential in T_1 values can be as large as 5 times. We emphasize that the nuclear T_1 (spin-lattice) relaxation here is not phonon mediated; instead, at the operational hyperpolarization fields, it originates predominantly from stochastic spin-flipping noise produced at ^{13}C sites from lattice paramagnetic electrons.^[32] This mechanism is dominant since the nuclear

Larmor frequency, $\omega_L = \gamma_n B_{\text{pol}}$ (for instance, $\approx 380 \text{ kHz}$ at 38 mT) can lie within the dipolar-broadened EPR linewidth. Specifically, the line broadening $\langle d_{ee} \rangle \approx \gamma_e \sqrt{\frac{8}{\pi}} \sqrt{M_{2e}} [\text{Hz}] \approx 10.5 P_e [\text{mG}]$, scales approximately linearly with electron concentration P_e ,^[33] where M_{2e} is the second moment of the electronic spectra^[34] $M_{2e} = \frac{9}{20} (g\mu_B)^2 \frac{1}{\langle r_e \rangle^6}$, and $g \approx 2$ is the electron g -factor, $\mu_B = 9.27 \times 10^{-21} \text{ erg G}^{-1}$ is the Bohr magneton, the inter-spin distance is $\langle r_e \rangle = (3/4\pi \ln 2)^{1/3} N_e^{-1/3}$, and $N_e = (4 \times 10^{-6} P_e)/a^3 [\text{m}^{-3}]$ is the electronic concentration in inverse volume units, and $a = 0.35 \text{ nm}$ the lattice spacing in diamond.^[33] Note that here we measure indirectly the cumulative effect of the paramagnetic spins on the ^{13}C nuclei and are agnostic to their exact lattice origin. The steep increase in relaxation rate in Figure 2D therefore reflects the deleterious increase in paramagnetic content on the ^{13}C nuclei, effectively increasing $\langle d_{ee} \rangle$ (see also Figure 3C).

Similarly, turning our attention to the extracted polarization injection rates (Figure 2E), we observe a saturation and decrease with increasing electron fluence. This is somewhat counterintuitive, since naively an increase in NV^- concentration should result in a greater number of sources seeding polarization into the ^{13}C lattice. However, the NV^- - ^{13}C polarization transfer is a coherent process, and Figure 2E strongly suggests that the transfer efficiency per MW sweep event is decreased in the higher fluence samples. This is potentially due to the reduction in NV^- center coherence time T_{2e} from interactions with the surrounding paramagnetic spin bath,^[35] as well as charge noise from lattice ionic nitrogen species.^[36] Figure 2 therefore illustrates that while would one like to electron irradiate samples to maximize the number of NV^- centers, this comes at a steep cost of lattice damage and paramagnetic impurity content, and strongly counteracts against ^{13}C hyperpolarization buildup.

4. High-Temperature Annealing Enabled DNP Gains

The samples considered so far were subjected to standard annealing, conditions that maximize optical fluorescence luminosity. On the other hand, annealing at higher temperatures could have a conciliatory role by relieving lattice disorder, due to the evolution and reorganization of defects.^[37,38] Motivated by this, we consider the effect of ultra-high temperature annealing on the hyperpolarization levels, employing a water-cooled annealing furnace (Figure 3A) that allows precise temperature control as well as rapid temperature rise times (see Methods in Supporting Information). While the annealing process constitutes a multidimensional parameter space dependent on temperature, annealing time, and sample environment conditions; here, we consider an important subset of these conditions, focusing on annealing in the $1700\text{--}1800^\circ\text{C}$ range, where NV^- centers can be preserved while paramagnetic content decreased^[39] (cf. Figure 4A).

We concentrate here on two representative classes of samples, those irradiated at i) $D_1 = 1.5 \times 10^{19} \text{ e cm}^{-2}$ (Figure 3B,C) that were optimally fluorescent in Figure 2C, and ii) at the maximum fluence level $D_2 = 5 \times 10^{19} \text{ e cm}^{-2}$ (Figure 3D,E), possessing close to the largest NV^- center concentration. Our observations (see Figure 3B,E showing mass normalized ^{13}C spectra) indicate that HTA in the $1700\text{--}1800^\circ\text{C}$ range can consistently lead to large

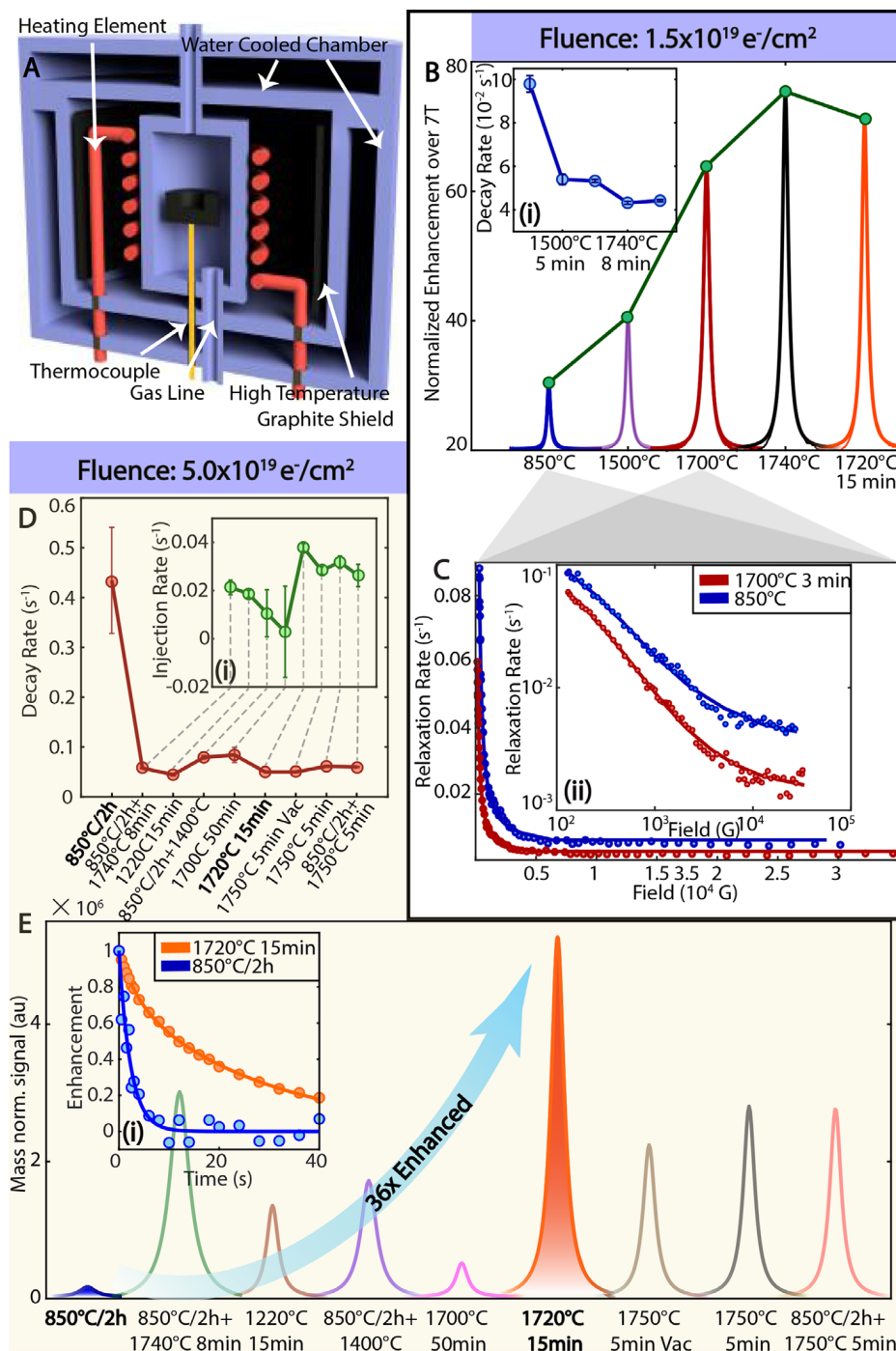


Figure 3. High thermal annealing (HTA) hyperpolarization gains. A) Home-built HTA furnace consisting of $\approx 1 \text{ cm}^3$ sample container and ability for precise control of temperature, annealing time, and environmental conditions. B) Mass-normalized ^{13}C NMR spectra for samples produced with fluence of $D_1 = 1.5 \times 10^{19} \text{ cm}^{-2}$, corresponding close to brightest particles (8 ppm NV^- concentration) in Figure 2A. HTA causes a $\approx 2.5\times$ increase in hyperpolarization levels compared to conventional annealing conditions (850°C). Inset (i): polarization decay rates, indicating that HTA conditions produce an $\approx 2.25\times$ increase in ^{13}C relaxation lifetimes. C) ^{13}C T_1 Relaxometry reveals the origins of this enhanced lifetime for a representative HTA sample. We map ^{13}C relaxation rates $R_1(B)$ over a wide field range 100 mT–3 T (Inset: data on log scale). Solid lines are fits to Tsallian functions (see Supporting Information). We observe a sharp narrowing of relaxometry profiles under HTA, manifesting in a increase in nuclear T_1 at all fields. D, E) Impact of HTA on high fluence samples with $D_2 = 5 \times 10^{19} \text{ cm}^{-2}$, originally corresponding to the worst performing sample in Figure 2A. D) Upper panel: Measured relaxation and injection rates under different HTA conditions, showing marked improvement in ^{13}C lifetimes. Inset: Extracted polarization injection rates, showing improvement in ^{13}C lifetimes by a factor $\approx 9\times$ under sample HTA. E) Lower panel: Mass-normalized spectra reveals a $\approx 36\times$ increase in the hyperpolarization enhancements under HTA over conventional annealing (blue arrow). While a wide range of HTA conditions can improve performance, optimal HTA conditions are found to be at $\approx 1720^\circ\text{C}$ for 15 min. Inset: Comparative ^{13}C relaxation decays at 38 mT, showing wide contrast in relaxation times with and without HTA.

improvements in the hyperpolarization levels over conventional annealing at 850 °C. For the D_1 samples (Figure 3B), HTA boosts polarization levels by ≈ 2.5 fold, while for the D_2 samples (Figure 3E), originally close to worst performing in Figure 2C, we find a large 36-fold increase (arrow in Figure 3E) in the magnitude of DNP enhancement levels under optimal 1720 °C HTA (shaded in Figure 3E). This allows these samples to leapfrog to the best overall for hyperpolarization despite initially showing very poor performance. If employed in ^{13}C hyperpolarized MR imaging,^[19] this would correspond to a substantial acceleration just by changes in the annealing conditions. These large gains are at once both surprising and technologically significant, since annealing at 1720 °C is not substantially more technically challenging than at 850 °C (Figure 3A),^[40] and time and temperature control opens new parameter spaces for lattice defect manipulation.

We notice moreover that a wide range of temperature conditions, anywhere in the 1200–1800 °C range, can yield substantial DNP improvements. Interestingly, short-time post-annealing a sample originally annealed at 850 °C at 1400 °C for 1 h can already increase DNP levels by 11-fold (fourth trace in Figure 3E). This points to the enhancement gains arising from lattice effects that are generally inaccessible under conventional annealing conditions. The data also reveals the importance of relatively rapid HTA, extended annealing, for instance, 50 min can lead to significantly degraded performance (fifth trace in Figure 3E). We observe that the exact environment of the annealing does not matter strongly, although a H_2 atmosphere is marginally better and can also serve to reduce diamond graphitization^[39] (Figure 3E). We note that the 36-fold increase in Figure 3E only quantifies the increase due to the rapid HTA considering identical starting samples at dose D_2 . It is interesting nonetheless that this optimal HTA sample, performs better than any of the samples considered in this study, 1.33 times better than the low dose (5×10^{18}) sample in Figure 2A. We anticipate that HTA will also benefit these latter samples. The best DNP performance corresponds to a bulk ^{13}C polarization $\approx 0.28\%$ (Figure 1A) and is the highest reported optical hyperpolarization level on crushed particles $< 20\ \mu\text{m}$ in size. Finally, the data in Figure 3B–D strongly indicate that these DNP signal boosts can be explained at least partially by the strong (≈ 2 –9 fold) increase in ^{13}C relaxation times as a result of HTA. This is most evident in the representative polarization decay curves in the inset of Figure 3E. We also observe a measurable increase in the polarization injection rates under HTA (inset in Figure 3D).

We now employ a combination of NMR relaxometry and quantitative EPR data to unravel lattice origins of these HTA-driven gains. Considering first the effect on increasing ^{13}C relaxation times, we find that this increase occurs across all magnetic fields (Figure 3C). To illustrate this, we use a recently developed NMR relaxometry method^[32] to quantify $R_1(B) = 1/T_1$, mapping the nuclear relaxation rates with magnetic field. Experiments are performed with a home-built field cyclor device,^[41] rapidly shuttling the sample to the field of interest where the spins are allowed to relax for a waiting period t , and subsequently detecting the polarization decay at 7 T. Stepping over values of t unravels the full T_1 decay curve at every field point, here with high precision (64 field points) over 100 mT–3 T (Figure 3C). In practice, we further accel-

erate the data acquisition using a dimension-reduction protocol outlined in ref. [32]. Fits to an exponential decay $\approx \exp(-t/T_1)$ allow extraction of field-dependent rates $R_1(B)$, which display characteristic step-like dependencies with field (shown in a linear scale in Figure 3C and log scale in the inset), growing steeply by over 2 orders of magnitude at low field and saturating beyond ≈ 100 mT to a relatively long T_1 value (≈ 10 min). The relaxometry profiles widths $\approx \frac{\langle d_{ee} \rangle}{2\gamma_n}$ report on the interactions of the ^{13}C nuclei with lattice paramagnetic spins.^[32] In these experiments, we cannot resolve differences between the exact paramagnetic spin species, but instead measure their net effect on the ^{13}C nuclei. The effects of HTA are now clearly evident (see Figure 3C); it leads to markedly modified NMR relaxometry profiles, narrowing them by $\approx 16\%$ even for the low fluence samples ($D_1 = 1.5 \times 10^{19} \text{ e cm}^{-2}$) considered. Our estimation here is based on the differences in the FWHMs of the two profiles. As a consequence, at any hyperpolarizing field, there is an increased time over which the ^{13}C polarization can buildup in the lattice, and consequently an enhanced saturation polarization level.

Complimentary aspects are revealed by X-band EPR spectra (see Figure 4), where we focus on the samples irradiated with the higher fluence $D_2 = 5 \times 10^{19} \text{ e cm}^{-2}$, since they present the largest relative gain in DNP levels in Figure 3. Figure 4A schematically displays the expected propagation of lattice defects under HTA conditions, and indicates the possibility of reducing radiation induced damage. We speculate that the HTA gains occur beyond the temperature corresponding to the offset of N diffusion ≈ 1500 °C, since some of the triplet defects might be associated with complexes of N and vacancies (Figure 4A). Consider first Figure 2C the case when the starting sample is annealed additionally at 1400 °C. The elevated temperature now causes the complete disappearance of W17-18 and W33 defects (top trace in Figure 2C), although at the cost of some reduction of NV^- concentration. The W16 content, on the other hand, remains practically unharmed in this case. Moving on to high-temperature annealing in the 1700–1800 °C range (dashed lines in Figure 4A), the effect on the triplet defects' content is even more pronounced (red trace in Figure 4B); most evident in the inset in Figure 4B that zooms into the spectral region near $g = 4.196$. The HTA treatment at 1720 °C completely eliminates all other e-beam induced triplet centers while only slightly affecting the NV^- content. Indeed, a fraction of the N atoms congregate into groups of 2–3 N atoms and combine with vacancies forming non-paramagnetic H3 and N3 color centers (Figure 4A). It is remarkable that the high NV^- density samples upon HTA treatment begin to resemble the triplet defect free spectra (second-to-last trace in Figure 2C) that characterize the samples at low electron fluence. The high NV^- concentration (≈ 4 ppm greater than Figure 2C) is now available free of adverse triplet paramagnetic content.^[42] In the Supporting Information, we present similar EPR spectra under a range of annealing conditions, showing progressive lattice quality improvement with annealing temperature. We note finally that post sample cleaning, we observe no EPR signatures of graphitization in the samples as a result of high-temperature annealing.

Annealing also affects the pool of primary defects, evident in the EPR spectra in Figure 4C (see Supporting Information): increasing the remanent substitutional nitrogen defects - P1

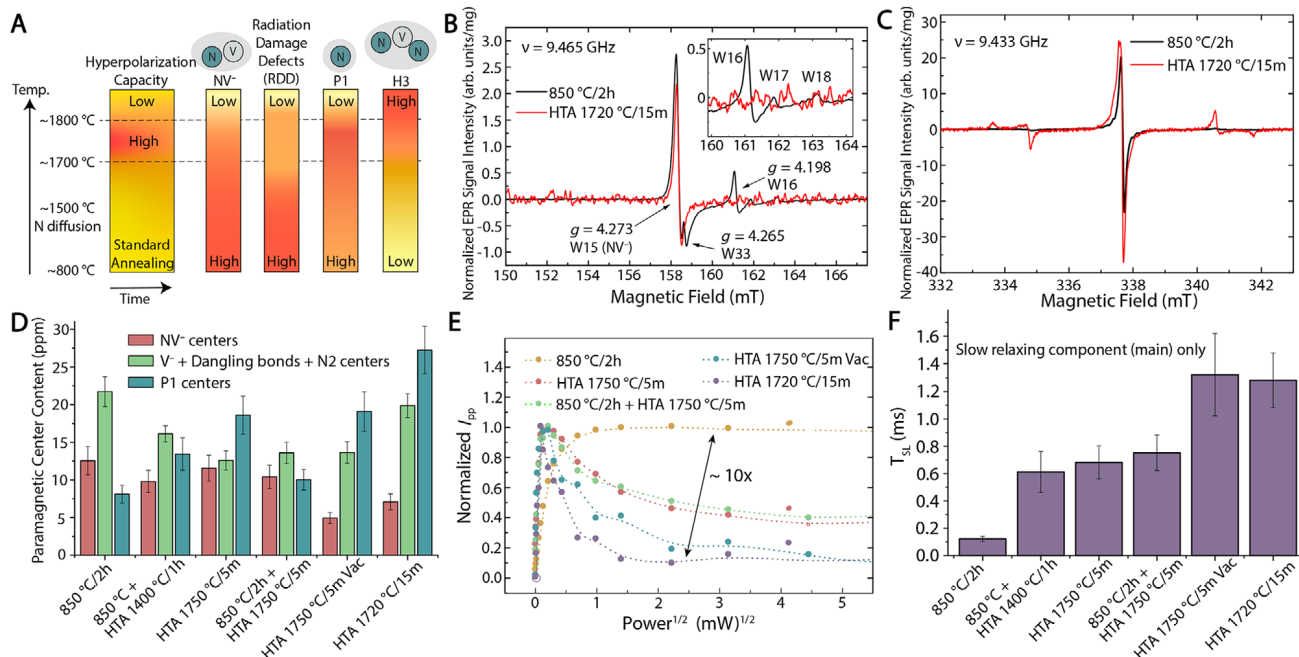


Figure 4. EPR spectra at X-band, revealing lattice origins of the HTA-driven hyperpolarization gains. A) Schematic of defect center evolution typical to HTA with changes in annealing time and temperature (axes). We target a HTA condition between 1700 and 1800 °C (dashed lines). B) EPR spectra at high electron fluence ($D_2 = 5 \times 10^{19} \text{ e cm}^{-2}$), displaying NV^- centers and spectrally closeby paramagnetic impurities (W33) centers (see also Supporting Information). HTA (red) suppresses the W33 and W16–W18 centers in its conventionally annealed counterpart (black). This manifests in EPR spectra similar to samples irradiated at low fluence (see Figure 2C). Inset: Zoom in on the accompanying triplet defect centers. C) P1 center EPR spectra shows an increase in P1 concentration under HTA, indicating lattice reorganization of nitrogen from N^+ to P1 (total nitrogen content in all samples is identical $\approx 100 \text{ ppm}$). D) Extracted concentrations of the $S = 1/2$, $3/2$ and $S = 1$ paramagnetic defects from the EPR spectra. E, F) NV^- spin-lattice relaxation times under several HTA conditions. E) Raw data MW saturation curves measured on the low field allowed transition in EPR spectra of NV^- centers (data for forbidden transitions in Supporting Information). F) Extracted T_{1e} times through exponential fit of the saturation curves in (E) (see Supporting Information for similar data on forbidden transitions). There is a boost of about an order of magnitude in electron T_{1e} in the 1720 °C HTA sample compared to conventional annealing.

centers (blue bars in Figure 4D), and modestly decreasing the content of negatively charged vacancies V^- , dangling bonds and N2 centers, deformation-produced dislocations decorated by nitrogen^[43] (green bars in Figure 4D). To explain this, we note that while the diamond samples considered here all have identical $\approx 100 \text{ ppm}$ of total nitrogen content; however, a predominant proportion manifest as N^+ ions that are not paramagnetic and hence are invisible in EPR. The increase in the P1 center concentration upon HTA, while a somewhat surprising observation, reflects the lattice reorganization from N^+ to P1 at high temperature. This likely serves to reduce the charge noise seen by the NV^- centers and can potentially contribute to their increased coherence times as well as T_{1e} lifetimes.

Indeed the most dramatic change upon HTA is found in the spin-lattice relaxation times of the NV^- centers (Figure 4E,F). We note that $\text{NV}^- T_{1e}$ is critical because at the relatively low laser illumination levels and slow MW sweeps, we employ (200 s^{-1}), it dictates the level to which the NV^- spins are polarized, ultimately bounds the ^{13}C nuclear polarization.^[17,44] T_{1e} times here are estimated by fitting progressive microwave saturation curves obtained for low-field allowed and forbidden ($g = 4.274$) lines of the NV^- EPR spectra, to a two-component model and assuming that the slow and fast relaxing entities originate from the same species. The saturation curves in Figure 4E (and Supporting Information) indicate that faster relaxing species become saturated

at higher MW power levels whereas sharp saturation peaks correspond to slower relaxing spins. It is evident in Figure 4E that HTA causes prolongation of spin-lattice relaxation times (see Supporting Information for related data on the forbidden transitions). The longest T_{1e} values, found for HTA 1750 °C (vacuum) and HTA 1720 °C treatments—and are about an order of magnitude longer than those conventionally 850 °C annealed (Figure 4F).

It emerges therefore from Figures 3 and 4 that the HTA enabled DNP gains arise from an interplay between increasing ^{13}C relaxation time by ≈ 2 to $9\times$, increasing NV^- center T_{1e} by $\approx 10\times$, as well a suppression in adverse triplet paramagnetic impurity content, all of which can be traced to HTA-driven “healing” of the diamond lattice disorder caused by radiation damage. Indeed, the best sample studied (HTA at 1720 °C) stands out with respect to its conventionally annealed counterpart; and is characterized by both a relatively high (7 ppm) NV^- content and a long $>1 \text{ ms}$ electron T_{1e} , as well as a complete absence of other e-beam induced triplet centers except for NVs. In contrast, the original 850 °C annealed sample had the highest content of remanent paramagnetic vacancies and secondary triplet centers, as well as the shortest T_{1e} values and only moderately higher NV^- content ($\approx 12 \text{ ppm}$). We anticipate that larger gains are possible through further optimization of the HTA process, and while demonstrated here for $18 \mu\text{m}$ particles, we expect these gains would also be translatable to nanodiamond samples.

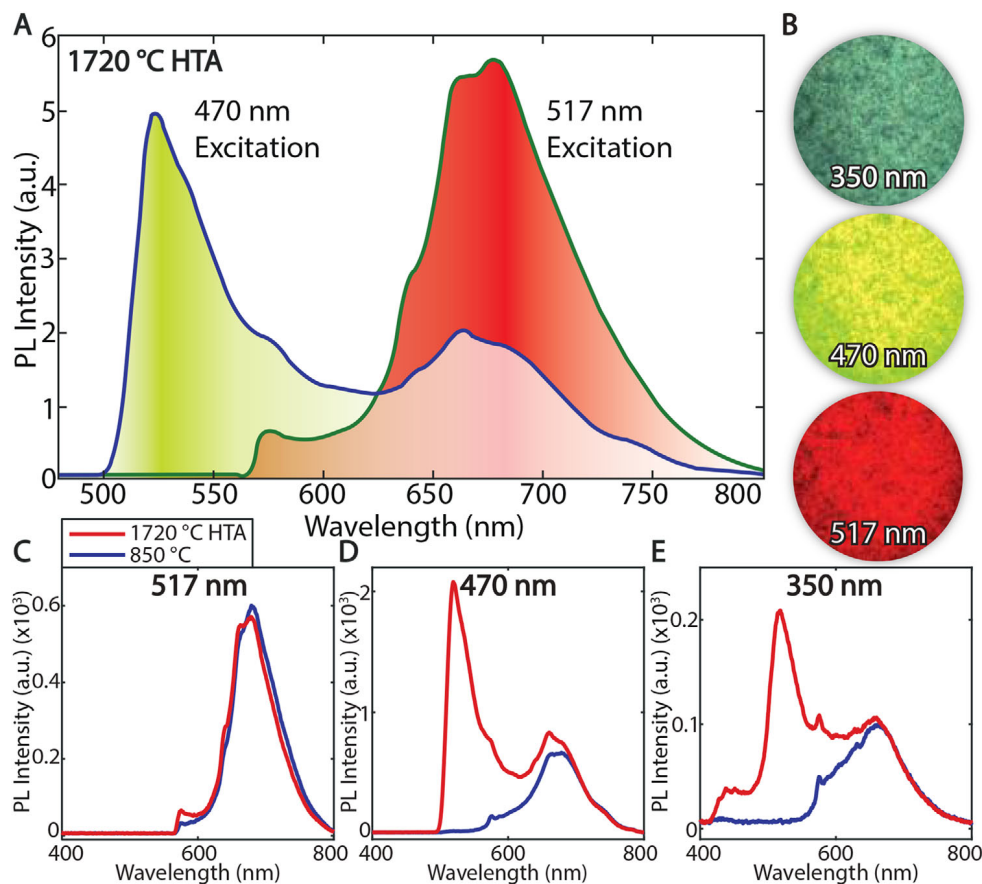


Figure 5. HTA driven multicolor diamond fluorescence. A) PL spectra measured for the HTA 1720 °C samples in Figure 3E studied under 470 nm and 517 nm excitation wavelengths, respectively, showing widely discriminated spectra. Shading indicates predominant fluorescence color. B) Multi-color fluorescence particle micrographs here for HTA 1720 °C samples. We employ excitations at 350 nm (UV), 470 nm (blue), and 517 nm (green), and image under 405 nm, 488 nm, and 561 nm long-pass filters, respectively. C–E) Comparison in PL spectra between HTA (red) and conventionally (blue) annealed samples, showing diversity of fluorescence color with excitation wavelength in the HTA case due to formation of nitrogen related defects. Conventional samples, in contrast, only predominantly fluoresce red.

5. Applications in Multimodal Imaging

Apart from enhanced hyperpolarization, HTA fortuitously also endows the particles with the surprising property of being fluorescent in more than one “color” under different excitation wavelengths.^[39] This effect arises due to the formation of NV[−], H3, and N3 centers, and mixtures thereof, conditional on and controllable via the annealing temperature. **Figure 5B**, for instance, demonstrates this for the best samples for hyperpolarization (HTA at 1720 °C), where the same particles glow in the dark-green, light-green, or red based on the UV (350 nm), blue (470 nm), or green (532 nm) excitation wavelengths. **Figure 5A** shows the measured PL spectra, displaying a wide separation in the dominant fluorescent wavelengths. **Figure 5C–E** highlights the strong differences to the conventionally annealed (850 °C) sample, wherein the PL is always predominantly in the red. We clarify however that HTA does not measurably enhance PL brightness from their values in **Figure 2B**, indicating that while DNP is more contingent strongly on the underlying lattice quality, while PL is more strongly conditioned on fluorescence quenching charge traps.^[45]

That said, however, the PL brightness is still substantial, and importantly, combined with natively high-contrast hyperpolarized ¹³C MR imaging that HTA-fabricated particles offer, multicolor optical imaging can allow new multimodal imaging avenues. Indeed, we envision the diamond particles being imaged under MRI as well as more than one optical wavelength simultaneously.^[19] This is aided by the fact that hyperpolarization can be carried out under any wavelength $\lambda \lesssim 575$ nm. Not only can imaging therefore proceed at the two widely disparate frequencies (RF and optical) simultaneously, but as we showed in recent work,^[19] exploiting the reciprocal space nature of optical and MR imaging can lead to substantial imaging acceleration in practical settings. In addition, both optical and MR modalities can be individually signal modulated on-demand, engendering lock-in techniques that can strongly suppress image backgrounds.^[19] It is in this context that the current work bears importance, since it provides a simple “materials-only” means to increase diamond ¹³C MR image signal-to-noise (SNR), while also concurrently allowing fluorescence in multiple optical channels, all of which portend approaches for high-fidelity particle tracking in vivo.^[46]

6. Conclusion

We have demonstrated the potential of high-temperature annealing toward boosting NV-center driven ^{13}C hyperpolarization in particulate diamonds at room temperature. At high NV^- concentrations, the use of HTA at 1720°C allows a boost in hyperpolarization levels by over an order of magnitude. We leveraged combined EPR and NMR techniques to systematically unravel origins of these surprising gains, studying DNP under several material dimensions including NV^- center concentration, annealing conditions, and particle size. It emerges that HTA serves to relieve radiation induced lattice disorder in the diamond lattice, reducing the triplet paramagnetic content, and increasing both the NV^- and ^{13}C T_1 lifetimes by factors approaching an order of magnitude each. Overall, this reveals the central role played by lattice quality in determining the final saturation ^{13}C hyperpolarization levels and suggests methods for the guided discovery of high-quality nanodiamond particles for enhanced spectroscopy and MR imaging. We anticipate that the lattice benefits from HTA will also translate to improved samples for quantum sensing and magnetometry,^[47,48] especially in the limit of high NV center densities. As such, this work complements recent work^[49] that demonstrated improvements in NV coherence times under high-temperature annealing, but highlights additionally the importance of both temperature and temporal axes in the annealing process. Finally, high-temperature annealing opens interesting opportunities for defect center manipulation, with potentially wider applications in quantum computing platforms in solids.^[50,51]

7. Experimental Section

Hyperpolarization at room temperature was carried out by nine fiber-coupled 520 nm laser diodes (Lasertack) at a 38 mT polarizing field generated by a pair of Helmholtz coils. A self shorted split-solenoid coaxial line connected to a 16 W MW amplifier provided the microwave excitation that initially consisted of frequency chirps generated from three cascaded voltage controlled oscillator (VCO) sources driven by a home-built quad ramp voltage generator.^[18] The diamond particles were immersed in water to leverage scattering-induced uniform illumination, as well as for heat sinking. DNP signals were measured in a 7 T Oxford magnet subsequent to sample shuttling to high field. This was achieved by a home-built field cycling stage consisting of a precise belt-driven actuator stage (Parker) with 50 μm precision.^[41] Shuttling times were measured to be ≈ 640 ms, small compared to ^{13}C nuclear T_1 .

Annealing of irradiated diamond powder in standard regime ($800\text{--}900^\circ\text{C}$) was done using a Blue Lindberg Model 848 furnace. Higher-temperature annealing was performed using an all-graphite furnace, model HTT-G10, MEO Engineering Company, adapted to treatment of diamond powder with a special graphite sample container (Figure 3A). Heating could be ramped up to the target temperature within minutes. For annealing of diamond powder at $1700\text{--}1800^\circ\text{C}$, the heating up time was about 3 min, then temperature was maintained for specified time at target temperature ($\pm 10^\circ\text{C}$) and followed by cooling down within 3 min to about 500°C and about 5 min for cooling down to room temperature. Temperature was measured using a W–Re thermocouple calibrated against melting points of pure Al, Au, Cu, Si, Ni, Pt, Pd, Rh, and Mo. In majority of experiments, HTA annealing was performed in hydrogen atmosphere. For a comparison in the experiment of annealing at 1750°C , both hydrogen and vacuum had been used.

Photoluminescence measurements in Figures 2B and 5 at room temperature were performed after each step of annealing. Analysis

was performed using an Olympus IX71 inverted fluorescent microscope and a modular USB spectrometer (HR2000, Ocean Optics). Excitation from a mercury lamp was filtered with a D350/50x band pass filter (Chroma) for UV excitation and BLP01-405R long pass emission filter (Semrock); FF01-470/28 (Semrock) bandpass filter for blue excitation measurements, with emission collected using a BLP01-488R (Semrock) long pass filter; and BLP01-532R (Semrock) bandpass filter for green excitation measurements, with emission collected using a BLP02-561R (Semrock) long pass filter. The microscope was also fitted with a 5.0 MP CCD color camera for simple color imaging applications (AmScope, MT5000-CCD-CK). Room temperature ($T = 295$ K) EPR measurements in Figure 4 were carried out at using a Bruker EMX-220 spectrometer equipped with an Agilent 53150A frequency counter.

Supporting Information

Supporting Information is available from the Wiley Online Library or from the author.

Acknowledgements

It is a pleasure to gratefully acknowledge discussions with B. Gilbert and D. Suter. This material is based in part upon work supported by the National Science Foundation Grant No. 1903803. Adamas acknowledges partial support from the National Cancer Institute of the National Institutes of Health under Award No. R43CA232901 and from the NHLBI, Department of Health and Human Services, under Contract No. HHSN268201500010C.

Conflict of Interest

UC Berkeley has filed a patent application related to this work (Ref: PCT/US 20/32700). Dr. Torelli and Dr. Shenderova work at small business company which sells fluorescent diamond particles. This has no bias on the reported scientific results.

Keywords

dynamic nuclear polarization, high-temperature annealing, hyperpolarization, NV centers

Received: May 15, 2020
Revised: August 22, 2020
Published online: September 9, 2020

- [1] J. M. Taylor, P. Cappellaro, L. Childress, L. Jiang, D. Budker, P. R. Hemmer, A. Yacoby, R. Walsworth, M. D. Lukin, *Nat. Phys.* **2008**, *4*, 810.
- [2] F. Dolde, H. Fedder, M. W. Doherty, T. Nobauer, F. Rempp, G. Balasubramanian, T. Wolf, F. Reinhard, L. C. L. Hollenberg, F. Jelezko, J. Wrachtrup, *Nat. Phys.* **2011**, *7*, 459.
- [3] P. Neumann, I. Jakobi, F. Dolde, C. Burk, R. Reuter, G. Waldherr, J. Honert, T. Wolf, A. Brunner, J. H. Shim, D. Suter, H. Sumiya, J. Isoya, J. Wrachtrup, *Nano Lett.* **2013**, *13*, 2738.
- [4] G. Kucsko, P. Maurer, N. Y. Yao, M. Kubo, H. Noh, P. Lo, H. Park, M. D. Lukin, *Nature* **2013**, *500*, 54.
- [5] M. Ledbetter, K. Jensen, R. Fischer, A. Jarmola, D. Budker, *Phys. Rev. A* **2012**, *86*, 052116.
- [6] A. Ajoy, P. Cappellaro, *Phys. Rev. A* **2012**, *86*, 062104.

- [7] F. Jelezko, J. Wrachtrup, *Phys. Status Solidi A* **2006**, 203, 3207.
- [8] V. N. Mochalin, O. Shenderova, D. Ho, Y. Gogotsi, *Nat. Nanotechnol.* **2012**, 7, 11.
- [9] M. Chipaux, K. J. van der Laan, S. R. Hemelaar, M. Hasani, T. Zheng, R. Schirhagl, *Small* **2018**, 14, 1704263.
- [10] L. P. McGuinness, Y. Yan, A. Stacey, D. A. Simpson, L. T. Hall, D. Maclaurin, S. Praver, P. Mulvaney, J. Wrachtrup, F. Caruso, R. E. Scholten, L. C. L. Hollenberg, *Nat. Nanotechnol.* **2011**, 6, 358.
- [11] D. Le Sage, K. Arai, D. R. Glenn, S. J. DeVience, L. M. Pham, L. Rahn-Lee, M. D. Lukin, A. Yacoby, A. Komeili, R. L. Walsworth, *Nature* **2013**, 496, 486.
- [12] Y. Wu, F. Jelezko, M. B. Plenio, T. Weil, *Angew. Chem., Int. Ed.* **2016**, 55, 6586.
- [13] R. Fischer, C. O. Bretschneider, P. London, D. Budker, D. Gershoni, L. Frydman, *Phys. Rev. Lett.* **2013**, 111, 057601.
- [14] T. R. Carver, C. P. Slichter, *Phys. Rev.* **1953**, 92, 212.
- [15] A. Abragam, M. Goldman, *Rep. Prog. Phys.* **1978**, 41, 395.
- [16] J.-H. Ardenkjaer-Larsen, G. S. Boebinger, A. Comment, S. Duckett, A. S. Edison, F. Engelke, C. Griesinger, R. G. Griffin, C. Hilty, H. Maeda, G. Parigi, T. Prisner, E. Ravera, J. van Bentum, S. Vega, A. Webb, C. Luchinat, H. Schwalbe, L. Frydman, *Angew. Chem., Int. Ed.* **2015**, 54, 9162.
- [17] A. Ajoy, K. Liu, R. Nazaryan, X. Lv, P. R. Zangara, B. Safvati, G. Wang, D. Arnold, G. Li, A. Lin, P. Raghavan, E. Druga, S. Dhomkar, D. Pagliero, J. A. Reimer, D. Suter, C. A. Meriles, A. Pines, *Sci. Adv.* **2018**, 4, eaar5492.
- [18] A. Ajoy, R. Nazaryan, E. Druga, K. Liu, A. Aguilar, B. Han, M. Gierth, J. T. Oon, B. Safvati, R. Tsang, J. H. Walton, D. Suter, C. A. Meriles, J. A. Reimer, A. Pines, arXiv preprint, arXiv:1811.10218, **2018**.
- [19] X. Lv, J. Walton, E. Druga, F. Wang, A. Aguilar, T. McKnelly, R. Nazaryan, L. Wu, O. Shenderova, D. Vigneron, C. A. Meriles, J. A. Reimer, A. Pines, A. Ajoy, arXiv preprint, arXiv:1909.08064, **2019**.
- [20] J. W. Aptekar, M. C. Cassidy, A. C. Johnson, R. A. Barton, M. Lee, A. C. Ogier, C. Vo, M. N. Anahtar, Y. Ren, S. N. Bhatia, C. Ramanathan, D. G. Cory, A. L. Hill, R. W. Mair, M. S. Rosen, R. L. Walsworth, C. M. Marcus, *ACS Nano* **2009**, 3, 4003.
- [21] G. C. Costa, O. Shenderova, V. Mochalin, Y. Gogotsi, A. Navrotsky, *Carbon* **2014**, 80, 544.
- [22] D. Abrams, M. E. Trusheim, D. R. Englund, M. D. Shattuck, C. A. Meriles, *Nano Lett.* **2014**, 14, 2471.
- [23] O. A. Shenderova, A. I. Shames, N. A. Nunn, M. D. Torelli, I. Vlasov, A. Zaitsev, *J. Vac. Sci. Technol., B: Nanotechnol. Microelectron.: Mater., Process., Meas., Phenom.* **2019**, 37, 030802.
- [24] M. H. Alkahtani, F. Alghannam, L. Jiang, A. A. Rampersaud, R. Brick, C. L. Gomes, M. O. Scully, P. R. Hemmer, *Opt. Lett.* **2018**, 43, 3317.
- [25] Y.-R. Chang, H.-Y. Lee, K. Chen, C.-C. Chang, D.-S. Tsai, C.-C. Fu, T.-S. Lim, Y.-K. Tzeng, C.-Y. Fang, C.-C. Han, H.-C. Chang, W. Fann, *Nat. Nanotechnol.* **2008**, 3, 284.
- [26] P. Reineck, M. Capelli, D. Lau, J. Jeske, M. Field, T. Ohshima, A. Green-tree, B. Gibson, *Nanoscale* **2017**, 9, 497.
- [27] L. B. Casabianca, A. I. Shames, A. M. Panich, O. Shenderova, L. Frydman, *J. Phys. Chem. C* **2011**, 115, 19041.
- [28] J.-P. Boudou, P. A. Curmi, F. Jelezko, J. Wrachtrup, P. Aubert, M. Sen-nour, G. Balasubramanian, R. Reuter, A. Thorel, E. Gaffet, *Nanotechnology* **2009**, 20, 235602.
- [29] A. Ajoy, R. Nazaryan, K. Liu, X. Lv, B. Safvati, G. Wang, E. Druga, J. Reimer, D. Suter, C. Ramanathan, C. A. Meriles, A. Pines, *Proc. Natl. Acad. Sci. USA* **2018**, 115, 10576.
- [30] P. R. Zangara, S. Dhomkar, A. Ajoy, K. Liu, R. Nazaryan, D. Pagliero, D. Suter, J. A. Reimer, A. Pines, C. A. Meriles, *Proc. Natl. Acad. Sci. USA* **2019**, 116, 2512.
- [31] A. Shames, A. Panich, W. A. Kempirski, A. Alexenskii, M. Baidakova, A. Dideikin, V. Y. Osipov, V. Siklitski, E. Osawa, M. Ozawa, A. Vul, *J. Phys. Chem. Solids* **2002**, 63, 1993.
- [32] A. Ajoy, B. Safvati, R. Nazaryan, J. Oon, B. Han, P. Raghavan, R. Nirodi, A. Aguilar, K. Liu, X. Cai, X. Lv, E. Druga, C. Ramanathan, J. Reimer, C. Meriles, D. Suter, A. Pines, *Nat. Commun.* **2019**, 10, 5160.
- [33] E. Reynhardt, *Concepts Magn. Reson., Part A* **2003**, 19A, 20.
- [34] A. Abragam, *Principles of Nuclear Magnetism*, Oxford University Press, Oxford **1961**.
- [35] E. Bauch, C. A. Hart, J. M. Schloss, M. J. Turner, J. F. Barry, P. Kehayias, R. L. Walsworth, arXiv preprint, arXiv:1801.03793, **2018**.
- [36] M. Kim, H. Mamin, M. Sherwood, K. Ohno, D. Awschalom, D. Rugar, *Phys. Rev. Lett.* **2015**, 115, 087602.
- [37] D. Twitchen, M. Newton, J. Baker, T. Anthony, W. Banholzer, *Phys. Rev. B* **1999**, 59, 12900.
- [38] R. Jones, J. Goss, H. Pinto, D. Palmer, *Diamond Relat. Mater.* **2015**, 53, 35.
- [39] L. Dei Cas, S. Zeldin, N. Nunn, M. Torelli, A. I. Shames, A. M. Zaitsev, O. Shenderova, *Adv. Funct. Mater.* **2019**, 29, 1808362.
- [40] S. Eaton-Magaña, T. Ardon, A. M. Zaitsev, *Diamond Relat. Mater.* **2017**, 77, 159.
- [41] A. Ajoy, X. Lv, E. Druga, K. Liu, B. Safvati, A. Morabe, M. Fenton, R. Nazaryan, S. Patel, T. F. Sjolander, J. A. Reimer, D. Sakellariou, C. A. Meriles, A. Pines, *Rev. Sci. Instrum.* **2019**, 90, 013112.
- [42] J. Goss, P. Briddon, R. Jones, S. Sque, *Diamond Relat. Mater.* **2004**, 13, 684.
- [43] R. Mineeva, S. Titkov, A. Speransky, *Geol. Ore Deposits* **2009**, 51, 233.
- [44] A. Jarmola, V. Acosta, K. Jensen, S. Chemerisov, D. Budker, *Phys. Rev. Lett.* **2012**, 108, 197601.
- [45] A. I. Shames, A. I. Smirnov, S. Milikisiyants, E. O. Danilov, N. Nunn, G. McGuire, M. D. Torelli, O. Shenderova, *J. Phys. Chem. C* **2017**, 121, 22335.
- [46] N. Whiting, J. Hu, J. V. Shah, M. C. Cassidy, E. Cressman, N. Z. Mill-ward, D. G. Menter, C. M. Marcus, P. K. Bhattacharya, *Sci. Rep.* **2015**, 5, 12842.
- [47] D. Le Sage, L. M. Pham, N. Bar-Gill, C. Belthangady, M. D. Lukin, A. Yacoby, R. L. Walsworth, *Phys. Rev. B* **2012**, 85, 121202.
- [48] T. Wolf, P. Neumann, K. Nakamura, H. Sumiya, T. Ohshima, J. Isoya, J. Wrachtrup, *Phys. Rev. X* **2015**, 5, 041001.
- [49] J.-P. Tetienne, R. De Gille, D. Broadway, T. Teraji, S. Lillie, J. McCoe, N. Donschuk, L. Hall, A. Stacey, D. Simpson, L. Hollenberg, *Phys. Rev. B* **2018**, 97, 085402.
- [50] J. R. Weber, W. F. Koehl, J. B. Varley, A. Janotti, B. B. Buckley, C. G. Van de Walle, D. D. Awschalom, *Proc. Natl. Acad. Sci. USA* **2010**, 107, 8513.
- [51] A. Sipahigil, R. E. Evans, D. D. Sukachev, M. J. Burek, J. Borregaard, M. K. Bhaskar, C. T. Nguyen, J. L. Pacheco, H. A. Atikian, C. Meuwly, R. M. Camacho, F. Jelezko, E. Bielejec, H. Park, M. Loncar, M. D. Lukin, *Science* **2016**, 354, 847.